Jiawei Xu · Kyohei Ueda · Ryosuke Uzuoka

Evaluation of failure of slopes with shaking-induced cracks in response to rainfall

Abstract Centrifuge model tests on slopes subject to shaking and rainfall have been performed to examine the response of slopes with shaking-induced cracks to subsequent rainfall and evaluate the corresponding landslide-triggering mechanisms. The failure pattern of the slope subject to shaking and then rainfall was found different from that of the slope subject to only rainfall. When shaking caused cracks on the slope shoulder and rupture line below, the mobilized soil slid along the slip surface that extended to the rupture line, the main crack became the crown of the undisturbed ground once the slope was subject to a subsequent rain event, and the progression of the landslide was related to the rainfall intensity. During the landslide caused by light rainfall, the main scarp kept exposing itself in the vertically downward direction while the ground behind the main crack in the crack-containing slope remained undisturbed. The detrimental effect of cracks on soil displacement was more evident when the slope was exposed to heavy post-shaking rainfall, resulting in a rapid and massive landslide. Additionally, the volume of displaced material of the landslide, the main scarp area on the upper edge, and the zone of accumulation were larger in the crack-containing slope subject to heavy rainfall, in comparison with those in the crack-free slope. The deformation pattern of slopes with shaking-induced cracks during rainfall was closely related to rainfall intensity and the factor of safety provided a preliminary estimation of slope stability during rainfall. Moreover, even when subjected to the same rainfall, the slopes with antecedent shaking-induced cracks displayed different levels of deformation. The slope that experienced larger shaking had greater deformation under the following rainfall, and the shaking-induced slope deformation also controlled the slip surface location. Finally, the velocity of rainfall-induced landslide could be greatly influenced by the prior shaking event alone. Despite being under light rainfall, the slope that has encountered intense previous shaking exhibited an instant landslide.

Keywords Centrifuge tests · Shaking · Cracks · Rainfall · Slope · Landslide

Introduction

Earthquakes and rainfall are two common natural disasters causing landslides (Keefer 1984; Schuster et al. 1996; Crosta 2004; Sassa et al. 2015) in various mountainous areas worldwide. Earthquake-induced landslides mainly resulted from liquefaction of saturated deposits (Cornforth 2005; Sassa et al. 1996; Okada et al. 2000; Uzuoka et al. 2005; Wang et al. 2014; Egawa et al. 2018; Kameda et al. 2019), sliding of the main body on a plane of weakness (Chigira and Yagi 2006; Chigira 2012), or marginally stable slopes (Seed and Goodman 1964; Seed 1966; Ling and Chigira 2020). Studies on the seismic response of slopes or embankments to earthquakes were also carried out by different researchers using various methods including centrifuges model tests (Matsuo et al. 2002; Liang and Knappett 2017), numerical

simulations (Uzuoka et al. 2005; Xiong et al. 2014), and shaking table tests (Koga and Matsuo 1990; Matsumaru et al. 2012). Generally, rainfall infiltration into slopes increases pore water pressure or reduces soil suction (especially in unsaturated soil slopes); the continual drop of the shear strength of soil significantly contributes to the failure of slopes during rainfall. Studies on rainfall-induced landslides or slope stability during rainfall have been conducted in different ways such as numerical analyses on the slope stability during rain infiltration (Cho and Lee 2001; Qi and Vanapalli 2015; Cai and Ugai 2004; Sharma and Nakagawa 2010; Tian et al. 2017), large/small-scale model experiments (Wang and Sassa 2001; Montrasio and Valentino 2004; Sharma and Nakagawa 2010), field tests (Ng et al. 2003; Springman et al. 2013; Rahardjo et al. 2005; Chen et al. 2018), and centrifuge model tests (Take et al. 2004; Tamate et al. 2012; Bhattacherjee and Viswannadham 2018). These methods provided valuable guidance on landslide-related research and have been adopted by numerous researchers to investigate the response of slopes to earthquakes or rainfall.

The preceding studies mainly focused on landslides or slope stability under a single disaster (either earthquakes or rainfall). However, multiple natural disasters such as earthquakes and heavy rainfall pose a constant threat to some areas. The analyses of slopes or embankments with consideration of the combined geohazards are thus necessary for the prevention against landslides in these areas. The stability of slopes subject to earthquakes and the subsequent rainfall is part of the related issues that need to be addressed. In some cases, slopes with certain topographies or geological conditions have adequate stability under normal static conditions, but become unstable when struck by horizontal forces from earthquakes, incurring tension cracks or fissures on their surfaces rather than complete failures, making them vulnerable to the following possible rainfall. Increasing attention is being paid to this phenomenon since it has been reported in the past several earthquakes. For instance, in the 1995 Kobe Earthquake (Tomita et al. 1996), 1999 Chichi Earthquake (Hotta et al. 2005; Lin et al. 2004, 2006), 2005 Kashmir Earthquake (Owen et al. 2008; Khattak et al. 2010), 2008 Sichuan Earthquake (Tang et al. 2011), 2011 Tohoku Earthquake (Usui et al. 2013), and 2016 Kumamoto Earthquake (Geospatial Information Authority of Japan 2016), plenty of slopes did not display failure or slide after completion of earthquakes and only fissures and cracks were found on their surfaces, causing landslides during the next rainy seasons (Lin et al. 2004; Tang et al. 2011) or posing a great risk of slide remobilization or landslides because of possible rainfall later on (Owen et al. 2008; Sato et al. 2007; Khattak et al. 2010). It was speculated that post-earthquake rainfall led to the failure of slopes with fissures or cracks, accounting for landslides that entailed casualties and damage to different extents. However, the correlation between post-earthquake rainfall and landslide activation of slopes was mainly based on satellite or aerial images (Tomita et al. 1996; Lin et al. 2004,

2006; Tang et al. 2011; Usui et al. 2013) and the landslide-triggering mechanism was still not clarified. The impact of rainfall on both stability and failure patterns of slopes that have been subjected to pre-rainfall earthquakes has not been explicitly investigated yet, and the behavior of slopes with earthquake-induced cracks struck by the following rainfall needs to be examined in detail.

As there has been no reported field verification through measurements in similar landslides until now and numerical simulations on landslides in such complex situations are also deficient at present, laboratory experiments on small specimens are a promising tool providing direct observations through which the kinematics of slope failure can be investigated. In this study, physical experiments on model slopes were performed in the centrifuge where earthquakes and rainfall were simulated. The objectives were (1) to evaluate the failure-triggering mechanism of slopes subject to post-shaking rainfall and (2) to examine the differences between slopes with cracks and those without cracks in response to rainfall. Shaking-induced cracks on the slope surface were simulated, and the effect of cracks on the slope behavior during the subsequent rainfall was then investigated through the comparison between slopes with cracks and those without cracks. Moreover, the effect of shaking intensity on the response of slopes to the subsequent rainfall was then studied. Experimental results, including acceleration response, pore water pressure, landslide kinematics and pattern, and slope deformation, were the main subjects discussed in this paper.

Experimental methods

Centrifuge modeling principles and scaling laws

As full-scale tests in geotechnical engineering are usually time-consuming and laborious to prepare, tests on soil samples at a reduced scale are more attractive and often carried out instead. However, soil mechanical behavior is highly stress-dependent, so directly conducting tests on a reduced-scale model might not yield satisfying results due to its considerably smaller stress level. The centrifuge applies an increased "gravitational" acceleration to a physical model so that the identical self-weight stresses in the model and prototype are realized. The scale model of the prototype has macroscopic dimensions reduced by a factor N and the same mass density as the prototype. When it is subjected to a centrifugal acceleration equivalent to N times the Earth's gravity (g), the stress similarity can be achieved at homologous points in both model and prototype. This is the basic law for centrifuge modeling. In this study, centrifuge model tests on slopes subject to dynamic loading and/or rainfall were carried out. Dynamic loading was excited to model slopes on the shaking table, and rainfall was simulated by sprays from a rainfall simulator. All 1:50 scale model slopes illustrated in Fig. 1 were exposed to a centrifugal acceleration field equivalent to 50 g in the process of testing.

The hydro-mechanical behavior of unsaturated soil is described by partial differential force equilibrium equation and water continuity equation (Wu and Zhang 2009; Qi and Vanapalli 2015). Given the low hydraulic conductivity of the unsaturated soil, water flow was ignored during dynamic loading in this study.

The relationship between hydraulic conductivity and water saturation of Masado (the soil used for the centrifuge experiments) was
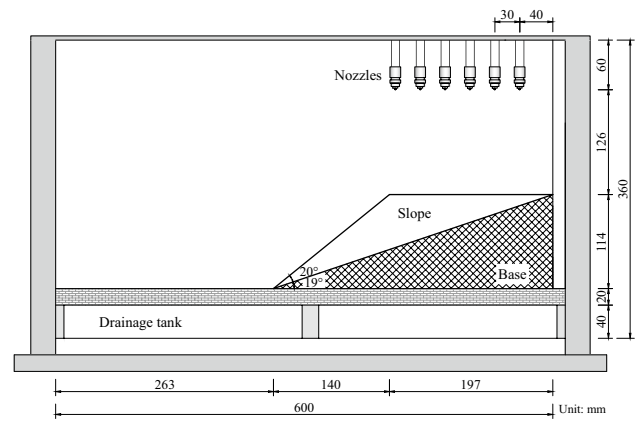

Fig. 1 Overview of model slope with rainfall simulator

obtained directly from SWCC experimental data by the method proposed by Jackson (1972), with results shown as scattered points in Fig. 2a. The equation proposed by Uzuoka and Borja (2012) was also utilized for the prediction of the unsaturated hydraulic conductivities over a large range of degrees of saturation. The formulation is given by
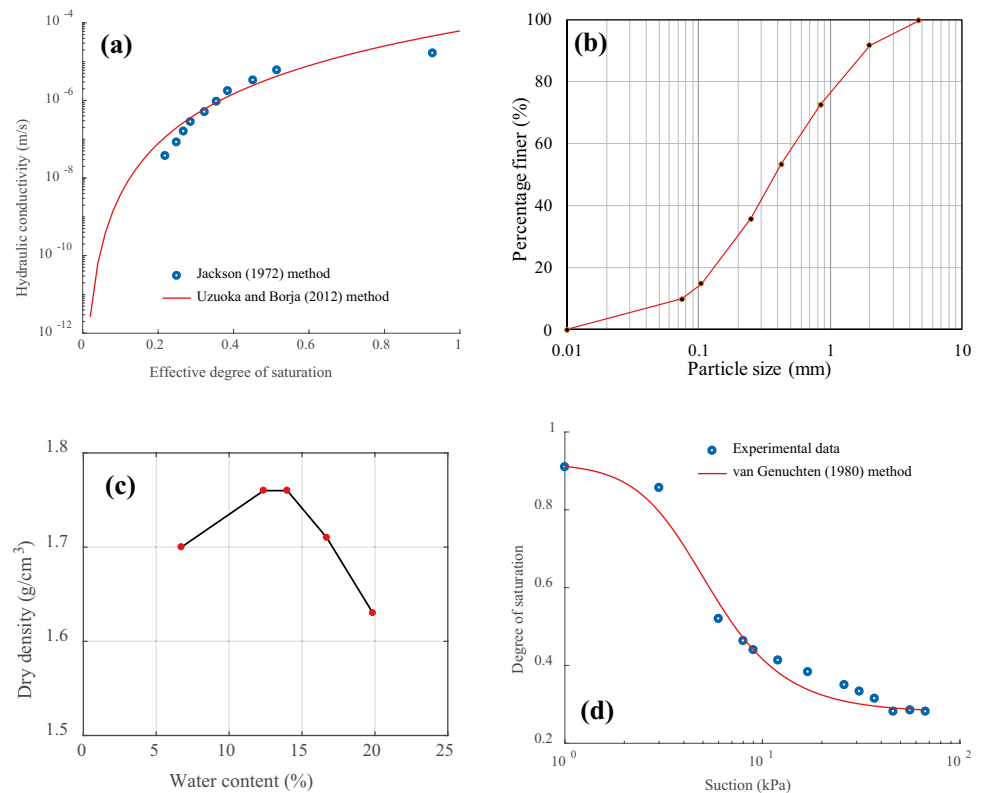
$$k^{\mathrm{ws}} = k_{\mathrm{s}}^{\mathrm{ws}} \left\{ s_{\mathrm{e}}^{\mathrm{w}} \right\}^{\xi_{\mathrm{vg}}} \left[1 - \left\{ 1 - \left(s_{\mathrm{e}}^{\mathrm{w}} \right)^{1/m_{\mathrm{vg}}} \right\}^{m_{\mathrm{vg}}} \right]^2 \qquad (1)$$

where $k_{\mathrm{s}}^{\mathrm{ws}}$ is the saturated hydraulic conductivity; $s_{\mathrm{e}}^{\mathrm{w}}$ is the efffective degree of saturation; ξ_{vg} and m_{vg} are material parameters equivalent to 0.5 and 0.63.

Since the effective degree of saturation of the soil sample was 0.17, the hydraulic conductivity was only in the order of 10^{-9} m/s. The low conductivity of the soil could prevent significant flow of water during shaking and the flow of water was not considered. According to Taylor (1995), the scale factors for time, acceleration, and frequency were taken as $1/N$, N, and N. According to Dell'Avanzi et al. (2004), the suction profile of the model was equal to that in the prototype when the ratio of the centrifuge arm length r_0 to the model height L_{m} was comparatively large (e.g., $r_0/L_{\mathrm{m}} > 10$). So the scale factor for suction was 1 (r_0/L_{m} ratio in this study is 22).

Once the slope was exposed to rainfall, seepage flow would have a time scale factor of $1/N^2$ in unsaturated soil (Dell'Avanzi et al. 2004; Rezzoug et al. 2004). However, the velocity of inertial events is the same in the model and prototype, indicating the velocity of a landslide in the model is equivalent to that in the prototype, so the time scale factor for inertial events is $1/N$ (Taylor 1995; Take et al. 2015; Bryant et al. 2015). The scale factor conflict between diffusion and inertial processes exists. Two possible strategies including using viscous fluid (Taylor 1995; Take et al. 2004; Zhang and Askarinejad 2019) or reducing grain sizes (Taylor 1995; Take et al. 2004) can be adopted to address the issue. Since water was used as the pore fluid for the models, the soil in the experiments here could be viewed as a material with larger grain sizes. However, the objective of this study was to examine the differences of the behavior of two types of slopes: slopes subject to shaking and then rainfall and slopes subject to only rainfall, instead of simulating particular prototype slopes in the field. In the experimental results, the time scale factor was taken as $1/N^2$ for converting the model time

Fig. 2 Properties of Masado soil: **a** relationship between hydraulic conductivity and effective degree of saturation, **b** particle size distribution, **c** compaction curve, and **d** SWCC

(a)

Jackson (1972) method
Uzuoka and Borja (2012) method

(b)

(c)

(d)

Experimental data
van Genuchten (1980) method

to prototype time during the rainfall phase. The main centrifuge scaling laws are listed in Table 1. It should be noted that, since the model test is a real event and the prototype is transformed from the model test results based on the scaling laws, special consideration is required when the conflict in time scale factors occurs. All results in this study were reported in the prototype scale unless otherwise stated.

Test program

Three series of tests (A, B, and C), eight tests in total, were performed at the centrifuge in the Geotechnical Centrifuge Center, Disaster Prevention Research Institute (DPRI), Kyoto University. This study aimed to examine the effect of shaking-caused cracks on the behavior of slopes in response to subsequent rainfall and investigate how shaking intensity and rainfall intensity would impact the performance of slopes during post-shaking rainfall.

The description of each model test is given in Table 2. Since the rainfall in test series A had a higher intensity than test series B and C, the terms "heavy rainfall" and "light rainfall" were used to differentiate between the two intensities. Upon the achievement of designated centrifugal acceleration of 50 g in tests A1 and B1, the inflight rainfall simulator was turned on in the container that accommodated the model slope, whereas shaking with a target intensity of 230 m/s² (4.6 m/s² in the prototype scale) was excited to the models in tests A2, A3, B2, and B3 prior to rainfall. Rainfall with two different intensities, 30 mm/h and 9 mm/h, was applied to test series A and B respectively. In test series C, however, upon the centrifugal acceleration of 50 g, rainfall with an intensity of 9 mm/h was released for the short period of time in each test and then

Table 1 Centrifuge scaling laws (N is the centrifugal acceleration)

Parameter	Dimension	Scale factor (model/ prototype)
Stress[a]	M/LT^2	1
Length[a]	L	$1/N$
Acceleration (dynamic)[a]	L/T^2	N
Frequency (dynamic)[a]	T^{-1}	N
Time (dynamic)[a]	T	$1/N$
Time (diffusion)[a]	T_{diff}	$1/N^2$
Time (inertial)[b]	T	$1/N$
Velocity (inertial)[b]	L/T	1
Rainfall intensity[c]	L/T_{diff}	N
Suction[d]	M/LT^2	1
Water flow rate[d]	L^3/T_{diff}	$1/N$
Discharge velocity[d]	L/T_{diff}	N
Hydraulic conductivity[e]	L/T_{diff}	N

[a] According to Taylor (1995)
[b] According to Taylor (1995), Take et al. (2004), and Bryant et al. (2015)
[c] According to Tristancho et al. (2012) and Tamate et al. (2012)
[d] According to Cargill and Ko (1983) and Barry et al. (2001)
[e] According to Barry et al. (2001) and Ng et al. (2016)

Table 2 Test program

Test	Target shaking intensity	Rainfall intensity	Description
A1	None	30 mm/h	Slope was subjected to only heavy rainfall
A2	4.6 m/s²	30 mm/h	Slope was subjected to shaking and then heavy rainfall
A3	4.6 m/s²	30 mm/h	Repeatability of test A2
B1	None	9 mm/h	Slope was subjected to only light rainfall
B2	4.6 m/s²	9 mm/h	Slope was subjected to shaking and then light rainfall
B3	4.6 m/s²	9 mm/h	Repeatability of test B2
C1	4.6 m/s²	9 mm/h	Slope was subjected to rainfall, intense shaking, and rainfall
C2	3.0 m/s²	9 mm/h	Slope was subjected to rainfall, moderate shaking, and rainfall

shaking with different intensities was given to tests C1 (4.6 m/s² in the prototype scale) and C2 (3.0 m/s² in the prototype scale), after which continuous rainfall with the same intensity was resumed until slopes failed.

Test series A and B were performed to study the effect of shaking-induced crest cracks on the response of slopes to the subsequent rainfall and how rainfall intensity would affect this process. Test series C were to investigate the impact of shaking intensity on the slope deformation and landslide kinematics during the post-shaking rainfall.

Model soil

Masado, which is decomposed granite soil commonly found in Japan and usually consists of a certain amount of silt, was used here to make model slopes.

The uniformity coefficient C_u and curvature coefficient C_c were calculated to be 7.46 and 1.01 from the particle size distribution curve of Masado in Fig. 2b; the fines content in the soil was roughly 10%. The soil was named well-graded sand with silt (SW-SM) according to the American Society for Testing and Materials classification system.

The compaction curve of the soil in Fig. 2c reveals a maximum dry density of 17.36 kN/m³ and optimum water content of 13%.

Laboratory test was performed to get the soil–water characteristic curve (i.e., SWCC) of Masado. Fig. 2d shows the experimental data and fitted curve by van Genuchten (1980) model with an equation written as

$$s_e^w = \frac{s^w - s_r^w}{s_s^w - s_r^w} = \left\{ 1 + \left(a_{vg} p^c \right)^{n_{vg}} \right\}^{-m_{vg}} \tag{2}$$

where s^w is the current degree of saturation; s_r^w and s_s^w are the residual and saturated degrees of saturation, which are 0.25 and 0.92; a_{vg}, n_{vg}, and m_{vg} are material parameters with values of 0.24 kPa⁻¹, 2.7, and 0.63.

The stepwise moist-tamping technique was employed to prepare soil specimens. Water instead of other viscous fluid was used as the experimental fluid to prepare model slopes and simulate rainfall in all the tests; this was because liquefaction was unlikely to take place in these slopes during shaking and fast water flow would not be

incurred. In the soil slope, the water content was 10%, the degree of saturation was 0.35, and the suction was nearly 20 kPa (according to SWCC in Fig. 2d). The saturated hydraulic conductivity of Masado was 4.4 mm/h. Once the compaction was completed, excess soil was scraped away. The model slope in the container is shown in Fig. 1.

Inflight rainfall simulator

An integrated system consisting of nozzles, an aluminum plate, pipes, valves, and pressure gauges was designed to produce rainfall in centrifuge experiments. The inflight rainfall simulator, which comprises assembled nozzles housed by the aluminum plate, was mounted on top of the container and could administer water drops to the model slope during the inflight testing process. Given that the width of the container accommodating the model slope was 14 cm, a total of 18 nozzles were arranged in three columns so that sprays from the nozzles could cover all the areas of the slope crest. Since a rain droplet in the centrifuge should be 50 times smaller than that in the prototype and natural rainfall rarely has rain droplets larger than 5 mm in diameter, air pneumatic nozzles were used on account of their capability to produce droplets with an average size of 20 to 100 μm. In addition, since soil erosion is related to the impact pressure of raindrops falling on the slope surface (Mhaske et al. 2019) and the impact pressure is affected by the raindrop size, reducing the raindrop size could greatly reduce the impact pressure (Tamate et al. 2012). The pneumatic nozzles used in the experiments were also able to alleviate the surface soil erosion during rainfall to a large extent. The water tank supplying water was welded to the container and the air cylinder was placed on the centrifuge arm to supply both air flow and water flow. A remote control was designed and used to switch on and off the solenoid valves in the integrated system so that the beginning and ending of rainfall could be realized in the inflight experiments.

The prerequisite for uniform rainfall produced by the inflight rainfall simulator is the same water pressure and air pressure feeding nozzles. Since air pressure was from one source (air cylinder), the same air pressure in each nozzle could be easily maintained. The water pressure in each nozzle should be the same to guarantee the same spray intensity in each nozzle. The hydraulic head in each nozzle was the vertical distance between the water surface in the

water tank and nozzle plus the imposed equal air pressure from the air cylinder. Therefore, if nozzles were placed the same vertical distance above the slope outline, nozzles above the downslope part would get a larger water pressure as the hydraulic head in those nozzles was larger than that of nozzles right above the slope crest. This would incur a non-uniform rainfall pattern and thus inaccurate experimental results. The main goal of this study was to investigate the effect of shaking-activated crest cracks on the behavior of the slope subject to post-shaking rainfall, so the flat crest area of the slope was the focus rather than the downslope part. Due to this, nozzles were fixed only above the flat slope crest as displayed in Fig. 1. In this way, it was also much easier to produce uniform rainfall because all the nozzles were at the same level and thus had the same water pressure and air pressure; the same spray intensity in each nozzle was guaranteed.

Calibration tests on nozzles were conducted to minimize the Coriolis effect. Since the rotation of the centrifuge is clockwise, sprays from nozzles have the tendency to move rightward while falling. Small cups placed under the nozzles were used to collect water in the calibration tests. Different arrangements of nozzles, including different spacing and heights of nozzles and different distances of nozzles from the right side of the container, were examined. The final arrangement shown in Fig. 1 was adopted since it ensured no extra flow along the right wall would occur. The flow of water along the front and back walls was avoided mainly by adjusting the heights of air pneumatic nozzles. In centrifuge calibration tests, different combinations of air pressure and water pressure in the rainfall system were used until the designated rainfall intensity was achieved; then, different heights of nozzles above the slope were checked until no flow of water along the wall was observed.

Instrumentation

Five pore water pressure transducers (Fig. 3a) buried inside of the model slope in different positions were used to measure pore water pressures. Since model slopes were initially unsaturated and high suction existed within them, tension transducers with high capability were required if suction has to be measured. Pressure transducers utilized here were only capable of measuring positive pore water pressures, so the readings of the transducers were initialized as zero right before rainfall was released in the tests.

One accelerometer (A0) was fixed on the bottom of the container to record the shaking motion, and another five accelerometers (A1–A5) were placed within different soil layers during the

model preparation. The positions of different accelerometers are illustrated in Fig. 3a.

Soil displacement during the tests was obtained by processing the digital images taken by a high-speed camera in front. The image analysis was performed by tracing markers through the digital images. Plastic markers with black circles in their centers were placed between soil and the front transparent wall of the container. The markers were completely dried before being placed between the front wall and soil. The lightweight square markers had a length of 5 mm and thickness of 1 mm. During the spin-up of the centrifuge (the process of the centrifugal acceleration rising from zero to 50 g), it was observed that the makers did not move, and due to the confining pressure provided by the soil, the markers were firmly attached to the soil. Moreover, since the front wall and the markers were smooth, the friction between them was negligible. Therefore, the markers could move along with soil during shaking and rainfall and the markers' movement could represent the movement of the points in the soil with the same positions as the markers. To maintain the precision of the analysis, the high-speed camera was mounted onto an aluminum frame in front of the container and positioned carefully to capture the whole soil during the tests. It was firmly fixed so that no deviation was induced even during shaking. Different adjustments to the camera lens in both dynamic and static trial tests were made in order to find the clearest view the camera could provide. The same configuration of the camera was utilized throughout all centrifuge experiments after the optimal arrangement of the camera was determined. In each test, 20 markers were placed on the slope profile, and the displacement of three points located in the lower, middle, and upper parts of the slope was selected for discussion of soil displacement in different parts of the slope. The layout of points on the slope profile is given in Fig. 3b.

Experimental results and discussion

Repeatability

Repeated tests have been carried out to verify the test results. Main results of tests A2 and B2 as well as their repeatability tests, A3 and B3, are presented in this section. They were the acceleration response during shaking and soil displacement during rainfall in four tests.

Figure 4a reports the maximum accelerations recorded in four tests. The acceleration response was consistent in each test. The recorded input accelerations in four tests had an averaged peak value of 4.64 m/s², and the differences between the recorded maximum accelerations and their average value were within ± 3.0%.
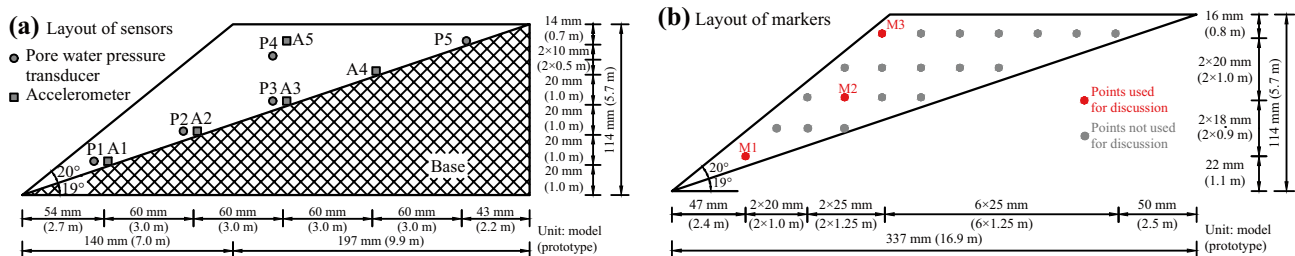

Fig. 3 Instrumented model slope: **a** layout of sensors and **b** layout of markers

The greatest peak acceleration was in A5 in each test. The averaged maximum acceleration of A5 in four tests was 6.50 m/s², and the differences between the recorded maximum accelerations and their average value were within ±1.8%. In addition, for A1, A2, A3, and A4, the differences between the recorded maximum accelerations and their average values fell within ±3.7%, ±2.8%, ±3.2%, and ±4.2%.

Soil displacement

Figure 4b, c plot the soil displacement during rainfall, with the downslope direction taken as positive in displacement. The soil displacement indicated similar results in the repeatability tests. In Fig. 4b, the soil displacement in tests A2 and A3 has very close initiation time (i.e., about 23 h since the onset of rainfall), and the upward trend soon after initiation was also drastic in both cases. In Fig. 4c, the initiation of slope displacement was also similar in tests B2 and B3, and the steady growth rate was seen in both cases.

Response of slopes to shaking

Acceleration response

Shaking in tests A2 and B2 could be regarded as repeated processes, because the initial slope condition and input motion in both tests were the same. The analysis of the slopes' response to dynamic loading in tests A2 and B2 was conducted prior to the discussion of slope behavior in the rainfall phase in four tests (tests A1 and A2, and tests B1 and B2).

The same sinusoidal shaking with a frequency of 50 Hz (1 Hz in the prototype scale) and a duration of 0.8 s (40 s in the prototype scale) was excited to the container on the shaking table once the

centrifugal acceleration went up to 50 g in both tests. The accelerations recorded at the bottom of the container and inside of both slopes are shown in the prototype scale in Fig. 5. The maximum input accelerations in two tests were 4.56 m/s² and 4.75 m/s². Two slopes had similar seismic response in terms of the wave form.

One noteworthy feature of the slopes during shaking was the peak acceleration amplification effect near their crests. The amplification effect in a slope was quantified by the amplification factor calculated as the peak acceleration at a given depth divided by the peak acceleration of the input motion (Liang and Knappett 2017). The amplification factor near the slope crest was taken as the ratio of the maximum acceleration recorded in A5 to the maximum input acceleration recorded in A0 in this study. Shaking greatly increased the induced accelerations near the crests of the slopes as shown by A5 in both Fig. 4a and Fig. 5. The maximum accelerations of A5 in tests A2 and B2 were 6.54 m/s² and 6.41 m/s² and the corresponding amplification factors were 1.43 and 1.35. Cracks were found on the crests of the slopes in both scenarios. However, trial tests on the slopes with the same initial condition showed that, when the maximum input acceleration was 2.90 m/s², the amplification factor was 1.16 and no crack was generated on the slope crest. Certainly, the amplification factor was directly related to the shaking intensity and slope failure could occur when the intensity was excessively large. The results here indicated that there might be a range within which shaking-induced tension cracks would occur on the slope crest. Further study of the correlation between amplification and shaking-caused damage to slope was needed, as it was relevant to the response of slopes to the subsequent rain event, which would be discussed in the following sections.
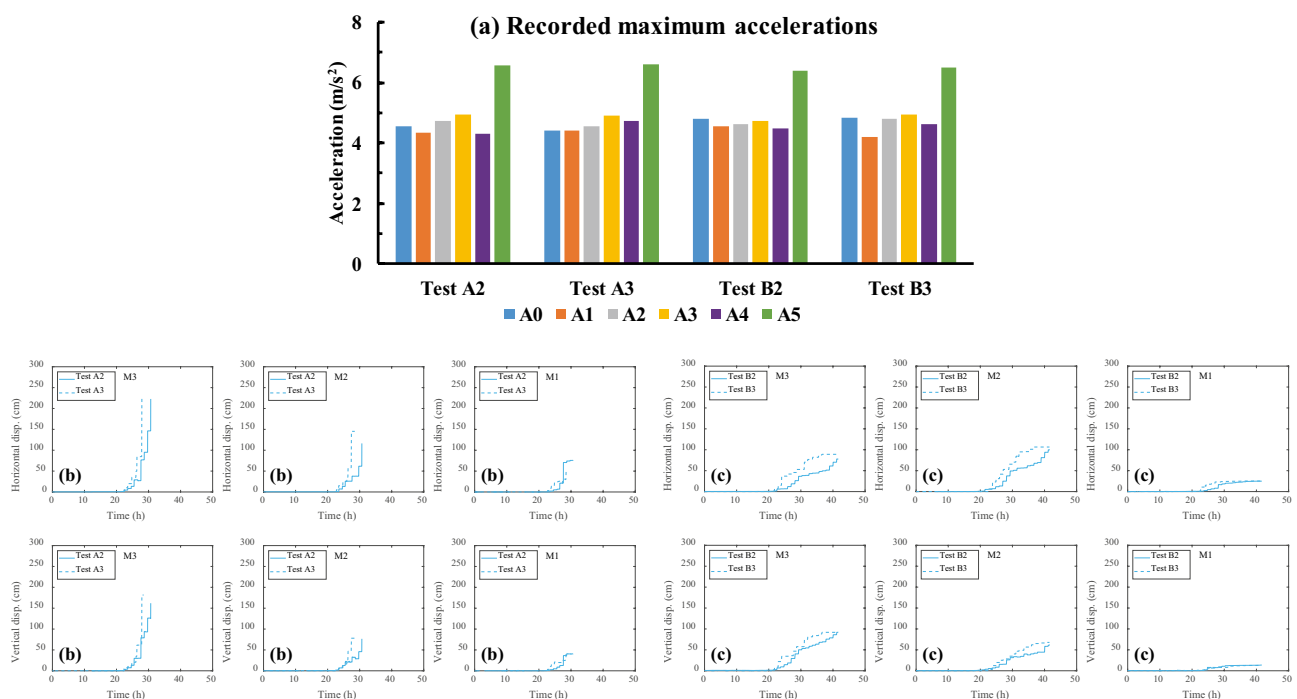

Fig. 4 Repeatability results: **a** maximum accelerations during shaking in tests A2, A3, B2, and B3; **b** soil displacement during rainfall in tests A2 and A3; **c** soil displacement during rainfall in tests B2 and B3
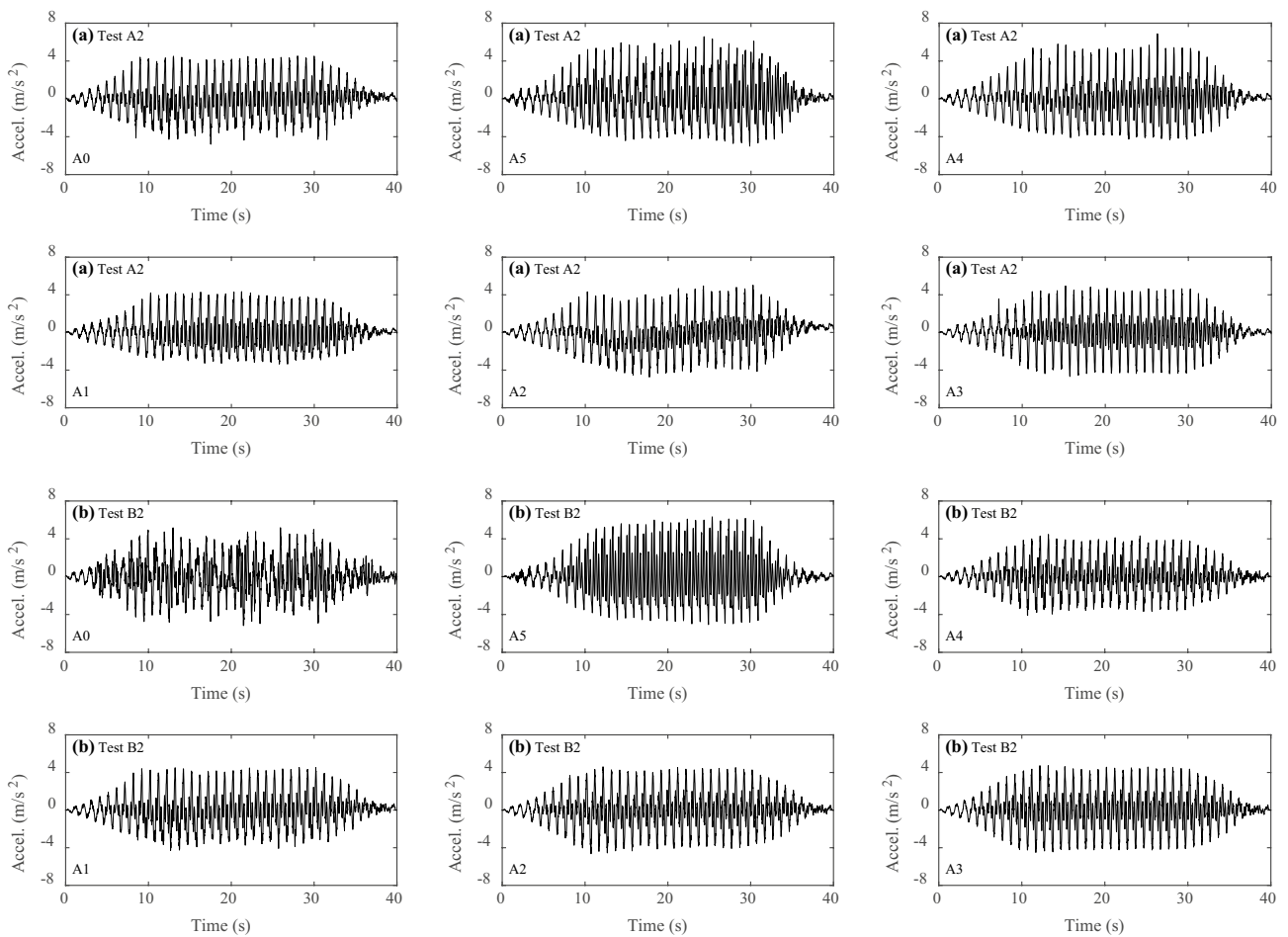
Fig. 5 Accelerations during shaking in tests A2 **a** and B2 **b**

Soil displacement

Figure 6a demonstrates the horizontal and vertical soil displacement over time in two slopes during shaking, where M1, M2, and M3 are located in different parts of the slope: the lower, middle, and upper parts. The displacement clearly showed the pattern of soil movement during shaking.

Let H/V be the ratio of the final horizontal displacement to the final vertical displacement after completion of shaking, then H/V had a clear downward trend from M1 (lower slope) to M3 (upper slope) in the magnitude, as shown in Fig. 6b. Additionally, the displacement vectors of the slopes after shaking are plotted in Fig. 7a, b, which provides a visual assistance in the understanding of the slope movement. The red line in Fig. 7a, b represents the slope surface after shaking, and the end of the red line on the slope crest shows the location of the main crack. Large soil displacement mainly took place in the left downslope part of the slope (in front of the main crack) while soil displacement behind the crack was very small.

Surface cracks

During shaking, the first crack that occurred on the slope crest was the one farthest away from the slope shoulder. As the soil moved in the downslope direction, more cracks started to gradually appear near the slope shoulder, and the last one was the one closest to the slope shoulder. The cyclic motion periodically widened and narrowed the cracks, leaving a final appearance of cracks manifested in Fig. 7c, d on the slope crest once it was ceased. Image analysis of the image captured by an overhead camera was performed to evaluate the distribution of cracks in the model slope in each test. A number of points on two edges of every major crack were selected and their coordinates in the frame were thus determined. In this way, crack distributions in Fig. 7c, d were obtained. The cracks in both model slopes were mainly distributed near shoulders, and the influencing range in the model slope in test B2 was slightly farther than that in test A2. As shown in the diagrammatic illustrations of cracks (Fig. 7c, d) after shaking, cracks were much closer to the front wall rather than the back wall. This was because the friction between the front transparent wall and soil was smaller than the friction between the back wall and soil, the cracks generated by shaking were more in quantity near the front wall. Since sensors in the slopes were placed along the parallel centerline between the front wall and back wall and image analysis of slope displacement was all based on the front view of the slope, the effect of friction disparity on the experimental results was lessened by these approaches.

However, the depth of the cracks was not visible during or after shaking despite the high-speed camera in front of the container to capture the slope motion. Although several crack lines were found
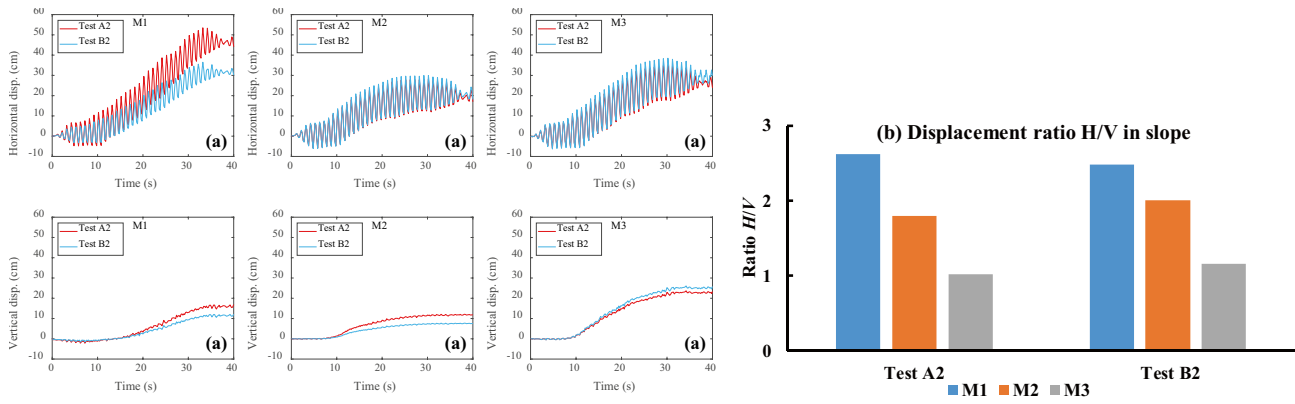
Fig. 6 Soil displacement during shaking **a** and displacement ratio *H/V* after shaking **b** in tests A2 and B2

on the surface, the main crack in tests A2 and B2 that influenced the landslides caused by rainfall in the next sections was the one farthest away from the slope shoulder, with a distance around 18 mm (0.9 m in the prototype scale). The width of each crack was not very distinguishable, and the image analysis indicated that the width of the main crack after shaking was approximately 0.8 mm, which would be 4 cm in the prototype scale.

Effect of shaking-induced cracks on the response of slope to rainfall with different intensities

Effect of shaking-induced cracks on pore water pressures

In test series A and B, rainfall with a high intensity (30 mm/h) and a low intensity (9 mm/h) was released above the models. Shortly

after rainfall was introduced to the container, positive pore water pressures (Fig. 8) inside of slopes gradually started to build up. The result of P1 in test A1 was absent due to its abnormal readings during the test. The highest and rightmost transducer P5 in each test initially exhibited an increase in pressure value since water could quickly accumulate around the area near P5 owing to its proximity to the seepage boundary provided by the base on which the slope rested.

The shaking-induced cracks in the slope in test A2 accelerated water flow during heavy rainfall since transducers P3 and P2 showed earlier increments compared with those in test A1, and the time discrepancies were a result of the presence of cracks on the slope shoulder. In Fig. 8a, transducer P3, which was located at the halfway point of the base, took approximately 13 h to display a positive value since the beginning of rainfall in test A1. While in the
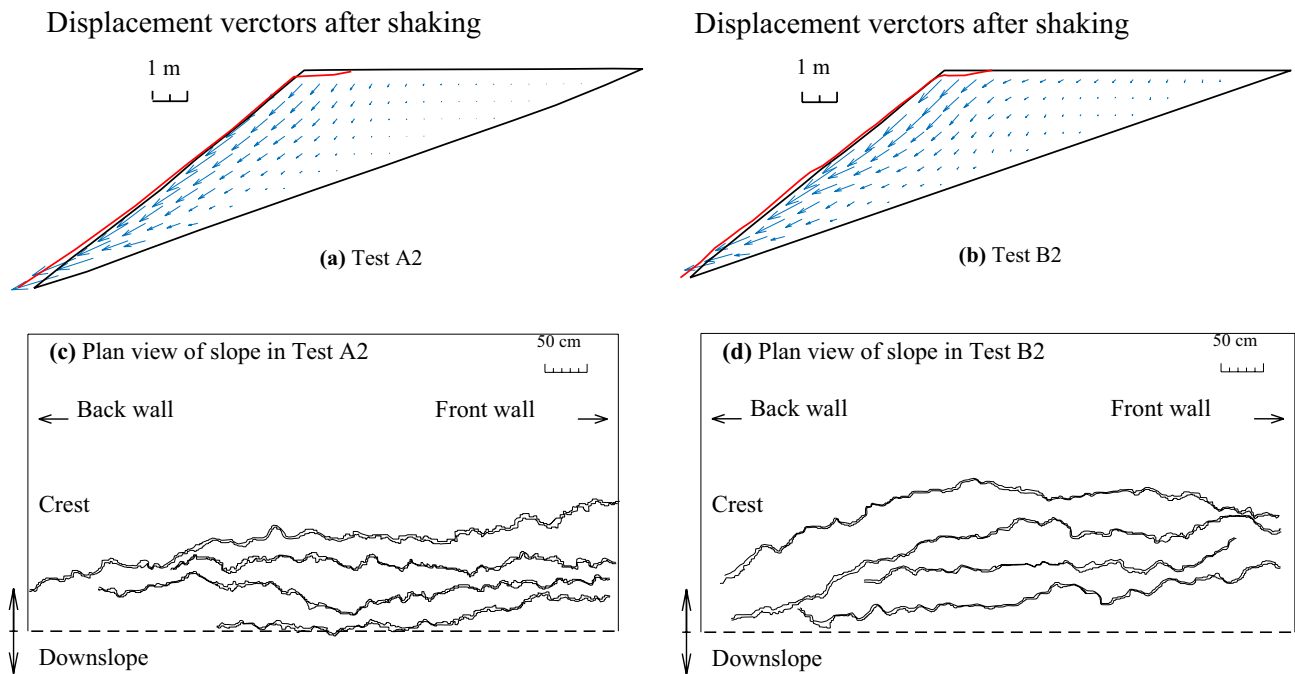

Fig. 7 Displacement vectors in slopes after shaking in tests A2 **a** and B2 **b** and diagrammatic illustrations of cracks on slope crests after shaking in tests A2 **c** and B2 **d**

slope with cracks in test A2 (Fig. 8b), P3 only took about 6 h for the same process. Also, the effect of preferential flow along cracks could be seen in the earlier response of transducer P2 in the downslope part in test A2 than its counterpart in test A1. The initiation time was about 17 h and 10 h respectively.

However, the impact of cracks on the time the pore water pressures in the downslope part took to increase was not significant under light rainfall, as shown in Fig. 8c, d. The time transducers P3 and P2 took to increase their positive values in both test B1 and test B2 had little difference. The pore water pressure response in test series A and B showed that the rainfall intensity could control how the shaking-induced cracks affected the speed of preferential flow.

Effect of shaking-induced cracks on landslide kinematics

Figure 9 provides the displacement of soil at three different locations in the slopes during rainfall. Landslide kinematic was analyzed based on the time history of soil displacement. The soil displacement had different patterns in two test series, and the effect of shaking-induced cracks on soil displacement depended on the rainfall intensity.

First, soil displacement of the slope during post-shaking heavy rainfall was larger, in comparison with that of the slope during heavy rainfall without antecedent shaking. According to the displacement of three different points in the slope throughout rainfall in Fig. 9a, the kinematic behavior of the slope subject to post-shaking rainfall in test A2 was distinct from that of the slope subject to only rainfall in test A1. The presence of cracks on the slope crest translated into a detrimental effect on the incidence of slope failure during heavy rainfall in test A2. The failure of the slope with shaking-induced

cracks during rainfall was abrupt, and the soil displacement was excessively greater compared with the slope subject to only rainfall.

Second, soil displacement of the slope during post-shaking heavy rainfall was faster, in comparison with that of the slope during heavy rainfall without antecedent shaking. According to the landslide velocity scale (Cruden and Varnes 1996), the landslide in test A2 had a velocity class between 6 and 7, suggesting a level between "very rapid (50 mm/s)" and "extremely rapid (5 m/s)", whereas the landslide velocity in test A1 fell within classes 4 and 5, suggesting a level between "moderate (0.005 mm/s)" and "rapid (0.5 mm/s)".

However, soil displacement of the slope during post-shaking light rainfall was similar, either in the magnitude or the velocity, to that of the slope during light rainfall without antecedent shaking. The difference of soil displacement between tests B1 and B2 was not discernible as shown in Fig. 9b. The growth rates of displacement in both slopes during rainfall were closely comparable. The travel speed of soil was in the order of 0.1 mm/s, indicating a level between "moderate (0.005 mm/s)" and "rapid (0.5 mm/s)". Further examination on the landslide features was still needed.

Landslide features

The progressions of landslides in centrifuge tests were captured by the front high-speed camera. The images of slopes after failure caused by rainfall are presented in Fig. 10. The outlines of slopes in different phases during rainfall in tests A1, A2, B1, and B2 are depicted in Fig. 11, in which the slope outlines are highlighted to show the progressions of landslides.
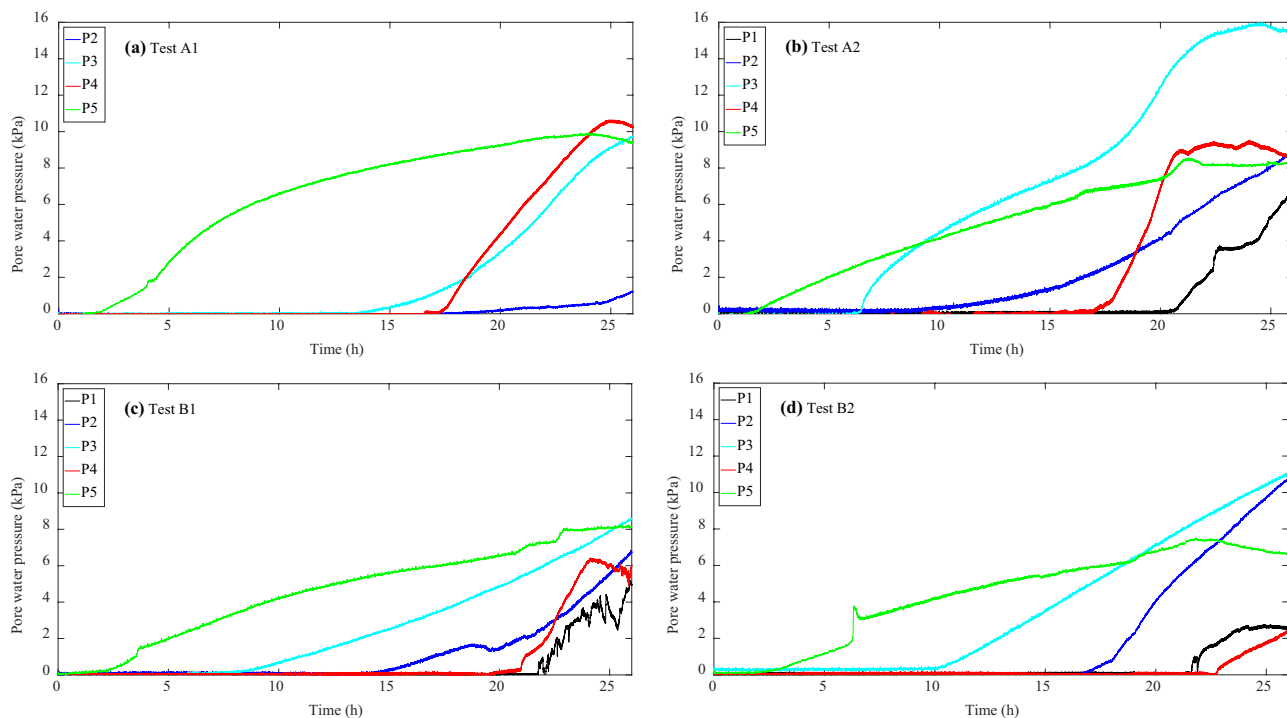

Fig. 8 Pore water pressures during rainfall: **a** test without shaking, A1; **b** test with shaking, A2; **c** test without shaking, B1; **d** test with shaking, B2
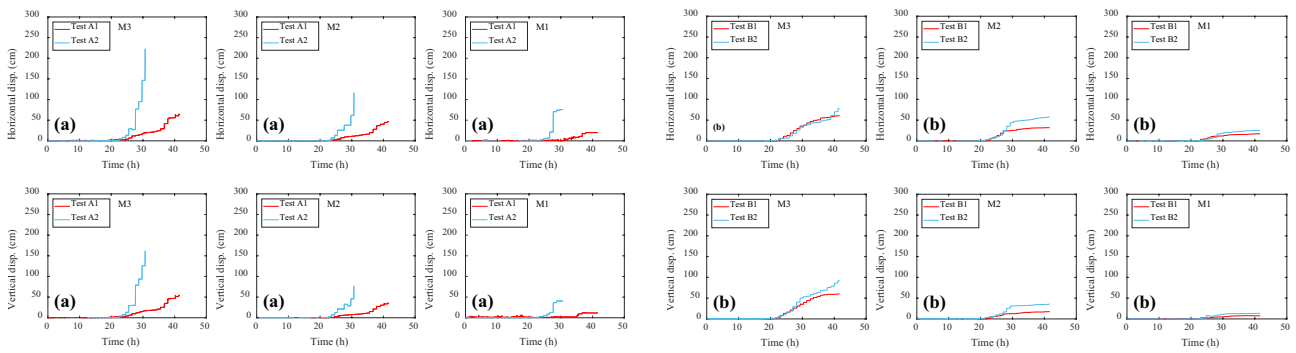
Fig. 9 Soil displacement during rainfall: **a** test without shaking, A1 and test with shaking, A2; **b** test without shaking, B1 and test with shaking, B2

Features of landslides caused by heavy rainfall

Compared with the failure of the slope (Fig. 11a) in test without shaking, the failure of the slope with shaking-induced cracks (Fig. 11c) during heavy rainfall had a different progression, with features including an increased exposure of the main scarp, a larger accumulation of displaced material, and a broader zone of depletion in the landslide.

Due to the presence of crest cracks, the soil before the cracks (toward the downslope side) moved at a faster pace than the soil behind the cracks initially. As indicated by the red line in Fig. 11c, the soil in front of the main crack settled more than the soil behind. As the landslide continued, more soil around cracks started to move, and more accumulated soil was found on the ground (blue line in Fig. 11c). The landslide's main scarp kept enlarging vertically, and the crown on the crest also retreated farther away from the original slope shoulder, causing a final slope profile in the green line in Fig. 11c.

The whole landslide process in the slope with cracks was fast. The duration of the initiation of landslide (red line in Fig. 11c) to the completion of landslide (blue line in Fig. 11c) was 7.7 h, whereas the duration for the slope in Fig. 11a was 23.1 h. The time difference was also reflected by the different growth rates of displacement of two slopes in Fig. 9a.

Features of landslides caused by light rainfall

Compared with the failure of the slope (Fig. 11b) in test without shaking, the failure of the slope with shaking-induced cracks (Fig. 11d) during light rainfall was different in progression. The landslide took place in front of the main crack, the exposed main scarp on the upper edge propagated vertically downward over time, and the soil behind the crack remained stable.

Soil movement in the slope with shaking-induced cracks was confined in front of the main crack, and the ground behind the main crack was stable throughout the test. 23.5 h since the beginning of rainfall, the surface soil was mobilized along the rupture line that underlay the main crack, and it was the precursor to a landslide. As presented in Fig. 11b, the depletion in the slope without cracks extended away from the slope shoulder, whereas in Fig. 11d, the depletion in the slope with cracks was evolving downslope and the soil behind the crack remained stable. After the slope failure, the zone of accumulation and zone of depletion in the crack-containing slope were slightly broader than those in the crack-free slope. However, as the mobilized soil gradually moved downslope along the slip surface that started from the rupture line, increasingly more accumulation of displaced soil was observed around the foot of the landslide and the main scarp kept exposing itself in the vertical downward direction, resulting in a final slope profile indicated by the green line in Fig. 11d.

Fig. 10 Slopes after failure caused by rainfall in tests without shaking, A1 **a** and B1 **b**, and tests with shaking A2 **c** and B2 **d**

(a) Test A1

(b) Test B1

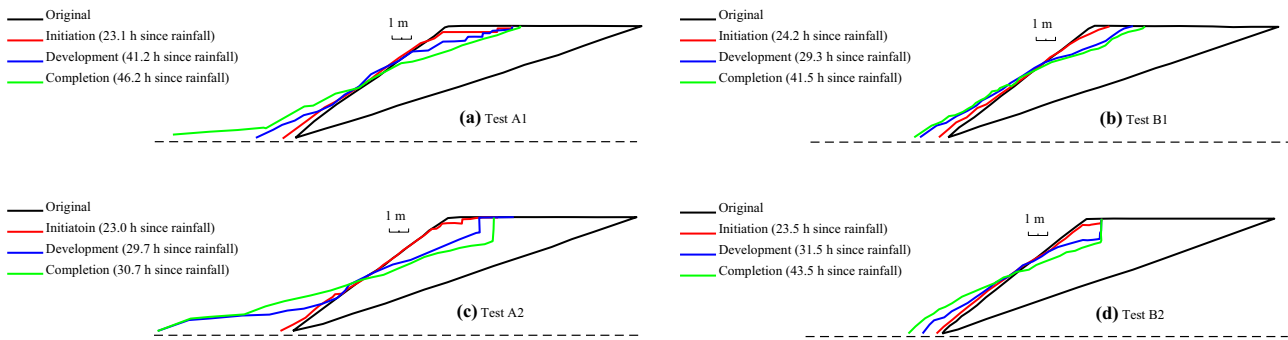**(c)** Test A2

(d) Test B2
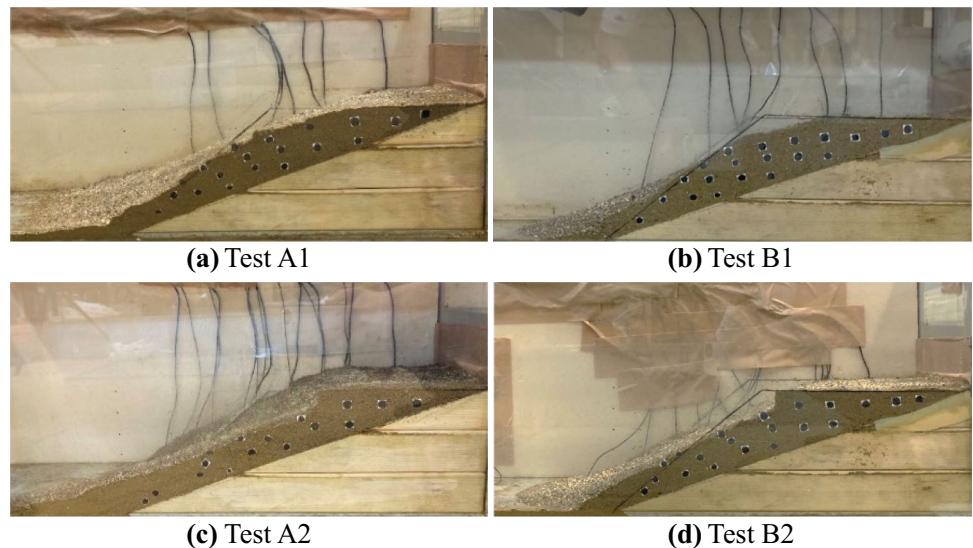
Fig. 11 Slope outlines during landslides caused by rainfall in tests without shaking, A1 **a** and B1 **b**, and tests with shaking A2 **c** and B2 **d**

Effect of rainfall intensity on the landslide features in slopes subjected to antecedent shaking

Rainfall intensity affected the landslide features of slopes with shaking-induced cracks. The main scarps in two slopes enlarged vertically in the early stage of the landslide, and the crown was defined by the main crack lines as indicated by the red lines in Fig. 11c, d, but the landslide patterns became different soon after that. As rainfall continued in both tests developed, the main scarp in the slope in test A2 continued to enlarge vertically and horizontally, whereas change in the main scarp was only vertical in the slope in test B2. This was also why the accumulation at the toe area in test A2 was much more, as indicated by the green and blue lines in Fig. 11c.

Rainfall intensity had a direct influence on the development of landslides in slopes with shaking-induced cracks. As a result of heavy rainfall, the occurrence of the landslide in test A2 was exceptionally rapid and the duration was significantly shortened, which were exemplified by its changing slope profile in Fig. 11c and high increment rate of displacement in Fig. 9a. However, rapid slope failure was not detected in the crack-containing slope under light rainfall in test B2, as shown by its slope profiles in Fig. 11d and low increment rate of displacement in Fig. 9b.

Slope deformation caused by rainfall
Further examination on slope deformation is presented in this section. Slope deformation could be evaluated by strain analysis. Since soil displacement during rainfall was already known from image analysis, the strains inside of the slope were determined by means of strain–displacement equations (Atkinson and Bransby 1978; Zhang et al. 2011). Since the centrifuge model tests were performed under the plane strain condition, the analysis involved only plane strains in x- and y-axis and strain components in z-axis were taken as zero. For a four-node equilateral element (Fig. 12), its normal and shear strain components are written as

$$\varepsilon_{xx} = \frac{1}{2a}\left(u_4 + u_1 - u_2 - u_3\right) \tag{3}$$

$$\varepsilon_{yy} = \frac{1}{2a}\left(v_2 + v_1 - v_3 - v_4\right) \tag{4}$$

$$2\varepsilon_{xy} = \frac{1}{2a}\left(\left(u_1 + u_2 - u_3 - u_4\right) + \left(v_1 + v_4 - v_2 - v_3\right)\right) \tag{5}$$

where ε_{xx}, ε_{yy}, and $2\varepsilon_{xy}$ are horizontal, vertical, and shear strains; u and v stand for horizontal and vertical nodal displacement, and the subscripts 1, 2, 3, and 4 represent the nodes 1, 2, 3, and 4 in the soil element; a is the length of the square element.

The equivalent strain ε_{eq} is defined as

$$\varepsilon_{eq} = \sqrt{\frac{2}{3}} \sqrt{\left(\varepsilon_{xx} - \frac{\varepsilon_v}{3}\right)^2 + \left(\varepsilon_{yy} - \frac{\varepsilon_v}{3}\right)^2 + \left(\varepsilon_{zz} - \frac{\varepsilon_v}{3}\right)^2 + 2\varepsilon_{xy}^2 + 2\varepsilon_{yz}^2 + 2\varepsilon_{zx}^2}$$
$$(6)$$

where ε_v is the volumetric strain and equals $\varepsilon_{xx} + \varepsilon_{yy} + \varepsilon_{zz}$. Given the plane strain condition, strain components ε_{zz}, ε_{yz}, and ε_{zx} are all zero.

Figure 13 provides the incremental equivalent strains at the onset of landslides caused by rainfall in four slopes in test series A and B. From the time when displacement started to develop until the same short period later, the incremental equivalent strains in four cases were taken for discussion. The localization of deformation could indicate the slip surfaces in four slopes. The deformation patterns in slopes exposed to rainfall and these exposed to post-shaking rainfall were different. The slip surfaces in tests A1 and B1 resembled the common failure surface for a homogeneous slope (Duncan et al. 2014; Huang 2014; Zhang et al. 2014) while the slip surfaces in tests A2 and B2 started near the slope toes and extended to a point below the slope crest and then became vertical. This was mainly resulted from the existence of shaking-caused crest cracks that changed the slip surface range. Since the slope was divided, once water filled up the cracks, the soil in front of cracks could displace easily due to the seepage force on the crack walls. The soil mass before the cracks then slid and formed a slip that terminated near the cracks. Apart from that, the deformation of slopes subject to rainfall after shaking was intensified, which could be seen from the magnitude. The difference in the slope deformation pattern between tests A2 and B2, though, was noticeable too. It was associated with the rainfall intensity as the pore water pressure (P4 in Fig. 8b) near the cracks in test A2 was higher than its counterpart (P4 in Fig. 8d) in test B2, causing larger deformation in soil near the cracks. That was also why the vertical boundary of the displaced soil mass was evident in the slope in test A2.

Slope stability during rainfall
Slope stability analysis is usually conducted through the assessment of the factor of safety (*FS*). The factor is calculated as the ratio
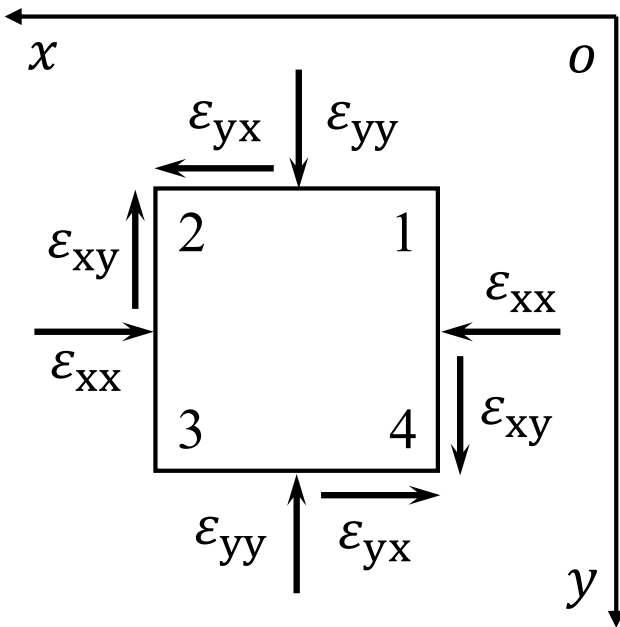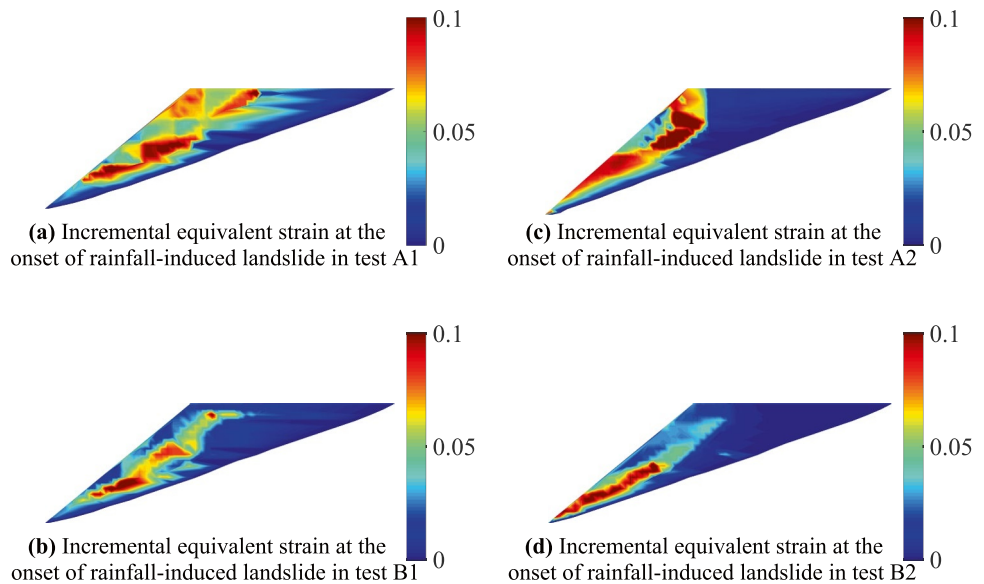
Fig. 12 Components of normal and shear strains in a soil element

The first component in Eq. 7 equals zero because of zero apparent cohesion c; the second component is constant and dependent on the friction angle φ and slip surface slope α; the third component varies with time because pore water pressure within the slope changes during rainfall.

The pore water pressure ratio (Bishop and Morgenstern 1960; Duncan et al. 2014) is calculated as

$$r_u = \frac{u_w}{\gamma_t h_s} \tag{8}$$

where u_w is the pore water pressure along the slip surface; γ_t is the unit weight of soil, which is 16.17 kN/m³; h_s is the depth of the slip surface below the slope surface.

Since FS varies with different slip surfaces chosen for investigation, a reasonably accurate determination of the slip surface location is generally necessary for the estimation of the slope stability evolution during rainfall. The analysis of FS could be conducted with the slip surfaces determined in the above section. As the slip surfaces in Fig. 13a, b were very close to planes, the simplified model in Fig. 14a could be used for FS analysis in tests A1 and B1 once the failure planes were confirmed. However, the analysis model for the stability of crack-containing slopes under rainfall was slightly different due to the different deformation patterns in tests A2 and B2 in Fig. 13c, d. As illustrated in Fig. 14b, c, one end point of the slip was at the slope toe, from where the slip extended to the slope crest in Fig. 14b or to a point below the slope crest and then vertically to the crest in Fig. 14c. In Fig. 14 b, c, α and β are 29° and 10°.

The detailed geometries of the slope models for analysis were obtained from Fig. 13. The calculation of FS for model in Fig. 14c was also based on Eq. 7 since the first part of the extreme-right-hand side in the equation was cancelled due to zero apparent cohesion and the second and third parts still held in both models. Due to the limited number of transducers, it was hard to acquire the pore water pressure in every point along the slip surface. As P1 and P4 were the closest to the slip surface in Fig. 14b, c, their values were used for the calculation of r_u. Once r_u in two points were calculated, their averaged value was substituted into Eq. 7.

between the downward driving force of the slope to its shear resistance, as shown in the triangular slope model in Fig. 14a. Consistent with previous studies (Duncan et al. 2014; Iverson 2000; Huang 2014), the factor of safety here has an expression of

$$FS = \frac{\frac{cH}{\sin\alpha} + N'\tan\varphi}{w\sin\alpha} = \frac{2\sin\beta/\sin(\beta-\alpha)(c/\gamma H)}{\sin\alpha} + \frac{\tan\varphi}{\tan\alpha} - r_u\frac{\tan\varphi}{\tan\alpha} \tag{7}$$

where W and H are the total weight and height of the slope; N' is the effective normal force; c is soil's apparent cohesion, which is zero according to the triaxial shear test; α and β are the angles of the slope and the slip surface; φ is soil's angle of friction, which is about 40° based on the triaxial shear test result; r_u is the pore water pressure ratio.

Fig. 13 Incremental equivalent strains at the onset of rainfall-induced landslides in test series A and B: **a** test A1 **b** test B1 **c** tTest A2 **d** test B2

(a) Incremental equivalent strain at the onset of rainfall-induced landslide in test A1

(c) Incremental equivalent strain at the onset of rainfall-induced landslide in test A2

(b) Incremental equivalent strain at the onset of rainfall-induced landslide in test B1

(d) Incremental equivalent strain at the onset of rainfall-induced landslide in test B2
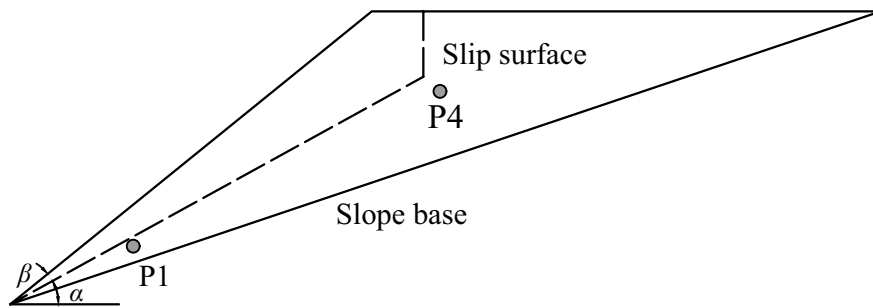
Fig. 14 Models for analysis of slope stability during rainfall. **a** A simplified triangular slope model with a plane failure surface. Model for analysis of slope stability during rainfall in **b** tests A1 and B1, and **c** tests A2 and B2
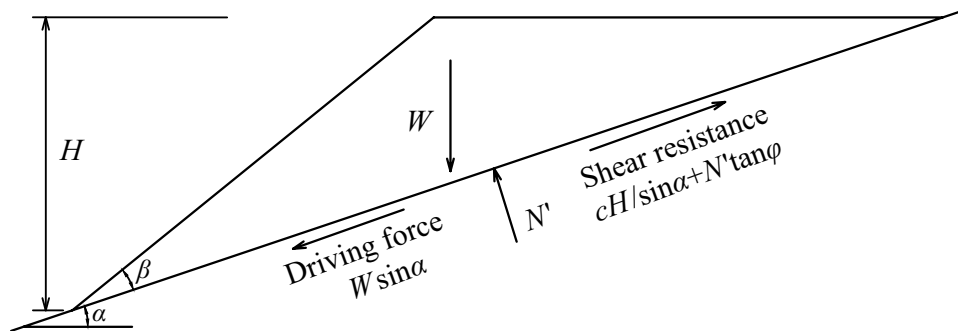
(a) A simplified triangular slope model with a plane failure surface
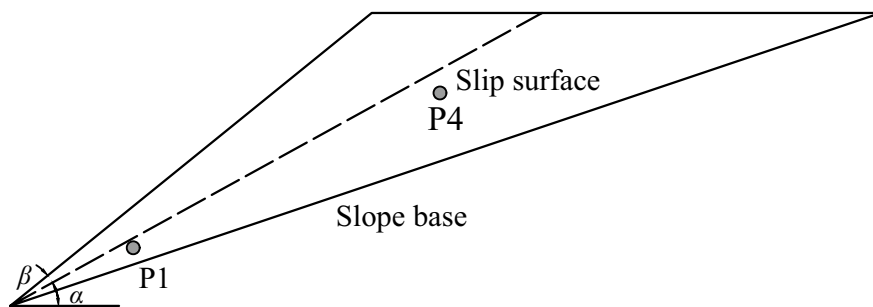
(b) Model for analysis of slope stability during rainfall in tests A1 and B1

(c) Model for analysis of slope stability during rainfall in tests A2 and B2

As to analytical solutions to slope stability during rainfall, pore water pressure (Conte and Troncone 2012) or factor of safety (Iverson 2000) was derived based on the infinite homogenous slope model in previous studies. These studies set out to solve Richards equation (Richards 1931; Fredlund and Rahardjo 1993; Bear 1972) and introduced some assumptions to facilitate the solving process. In this way, the relationship between the factor of safety and rainfall intensity was established. For the sake of comparison with the conventional method (Eq. 7), the analytical factor of safety (Iverson 2000) of slope during rainfall was also reported. It is given by

$$FS = \frac{\tan \varphi}{\tan \alpha} - \frac{\gamma_w}{\gamma_t} \frac{\tan \varphi}{\sin \alpha \cos \alpha} \frac{L_z}{K_s} \left(\sqrt{t^*/\pi} \exp(1/t^*) - \mathrm{erfc}\left(1/\sqrt{t^*}\right) \right)$$
(9)

where I_z is the rainfall intensity (30 and 9 mm/h in test series A and B); γ_w is the unit weight of water, which is 9.81 kN/m³; K_s is the saturated hydraulic conductivity (4.4 mm/h); erfc is the complementary error function; t^* is called normalized time equaling tD_0/Z^2, in which t is the time, and D_0 is the maximum hydraulic

diffusivity estimated to be 0.6 m/h from the ratio of the saturated hydraulic conductivity to the minimum specific moisture capacity; Z is the slip surface depth, which is taken as 2.5 m. It is noted that the analytical solution assumed a slip surface along the slope base; thus, the angle α in Eq. 9 was 19°, different from the one in Eq. 7, and *FS* had a different initial value compared to *FS* in other cases.

Figure 15 presents the development of *FS* in four cases under investigation. *FS* started to drop as the pore water pressures in Fig. 8 inside of slopes built up. For *FS* from the conventional method, a speedy growth in pore water pressures in test A2 led to the rapid falloff in the slope's *FS* during rainfall, whereas in other three cases, the reduction in *FS* was gradual. The results also corresponded to the rising soil displacement over time in Fig. 9 as *FS* decreased to near one or even less. It should be noted that, tests without shaking, A1 and B1, had very similar *FS* values when slopes failed, whereas tests with shaking, A2 and B2, showed discrepancies. This was because the effect of shaking such as the change in the angle of friction and pore water pressure distribution along the slip surface was not considered in this model. The conventional model performed

Fig. 15 Factor of safety of the slope during rainfall in test series A and B
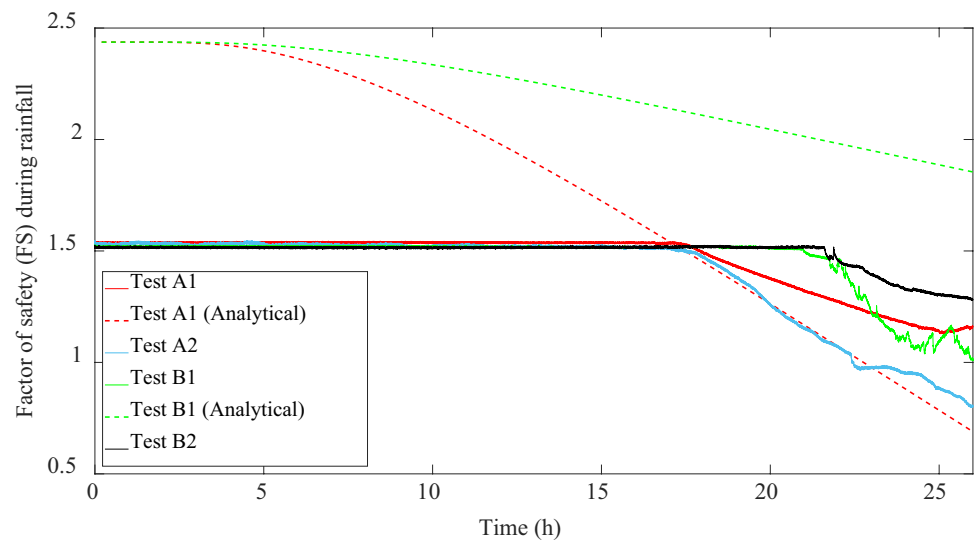
well in cases with only rainfall, but for cases with shaking and then rainfall, it needed improvement. Despite that, the decreasing trend of *FS* in four cases still provided assessment of slope stability during rainfall.
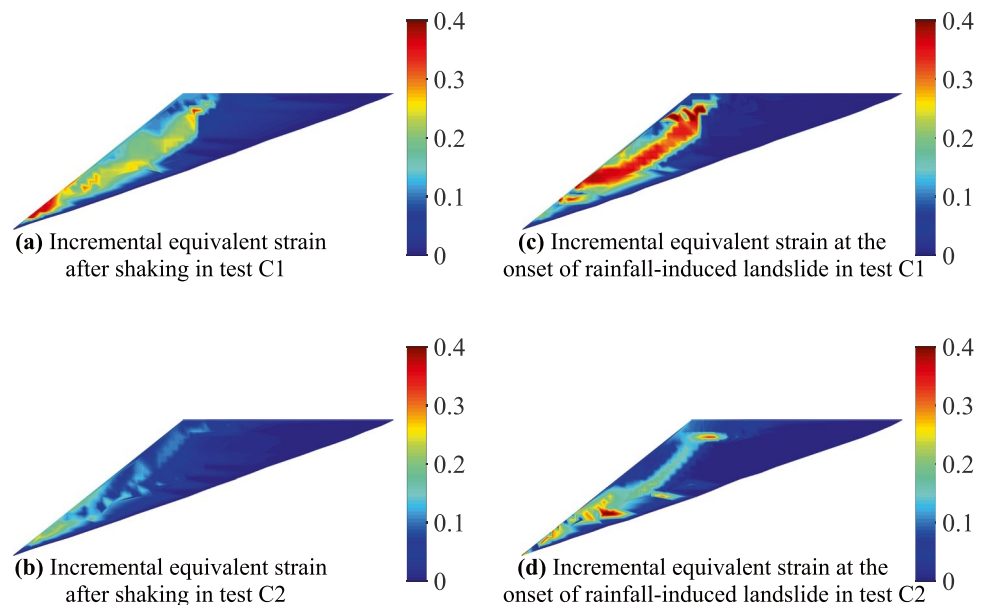
For the analytical *FS* in tests A1 and B1, though the decreasing trends were reflected, the disparity with others existed. The time from when *FS* started to drop was early, as it was about 5 h since the beginning of rainfall that *FS* reduced. The factor influencing the initiation time of *FS* reduction was the maximum hydraulic diffusivity D_0, so an accurate diffusivity value was important to capture this feature. Also, the analytical solution was based on the infinite-slope model with the slip surface along the slope base, which was different from the slope model in this study. This effect was more pronounced for the low-intensity case, where FS remained the largest as rainfall continued. The slip surface chosen for analysis should consider the rainfall, so that slope stability might be more reliable.

Therefore, the approximated *FS* of slopes during rainfall could be a preliminary estimate of slope stability, but a more detailed model was required for accurate analysis.

Effect of previous-shaking intensity on the slope deformation and landslide kinematics during the subsequent rainfall

The above sections discussed the effect of shaking-induced cracks on the slope behavior during the subsequent rainfall with different intensities. It was found that under shaking with a certain intensity, the effect of cracks on slope deformation and landslide kinematics during the following rainfall depended on the rainfall intensity. This section, however, is to investigate how shaking intensity would affect slope deformation and landslide kinematics during the rainfall subsequent to shaking.

Fig. 16 Incremental equivalent strains caused by shaking and its following rainfall in tests C1 and C2: **a** test C1 with shaking **b** test C2 with shaking **c** test C1 with rainfall **d** test C2 with rainfall
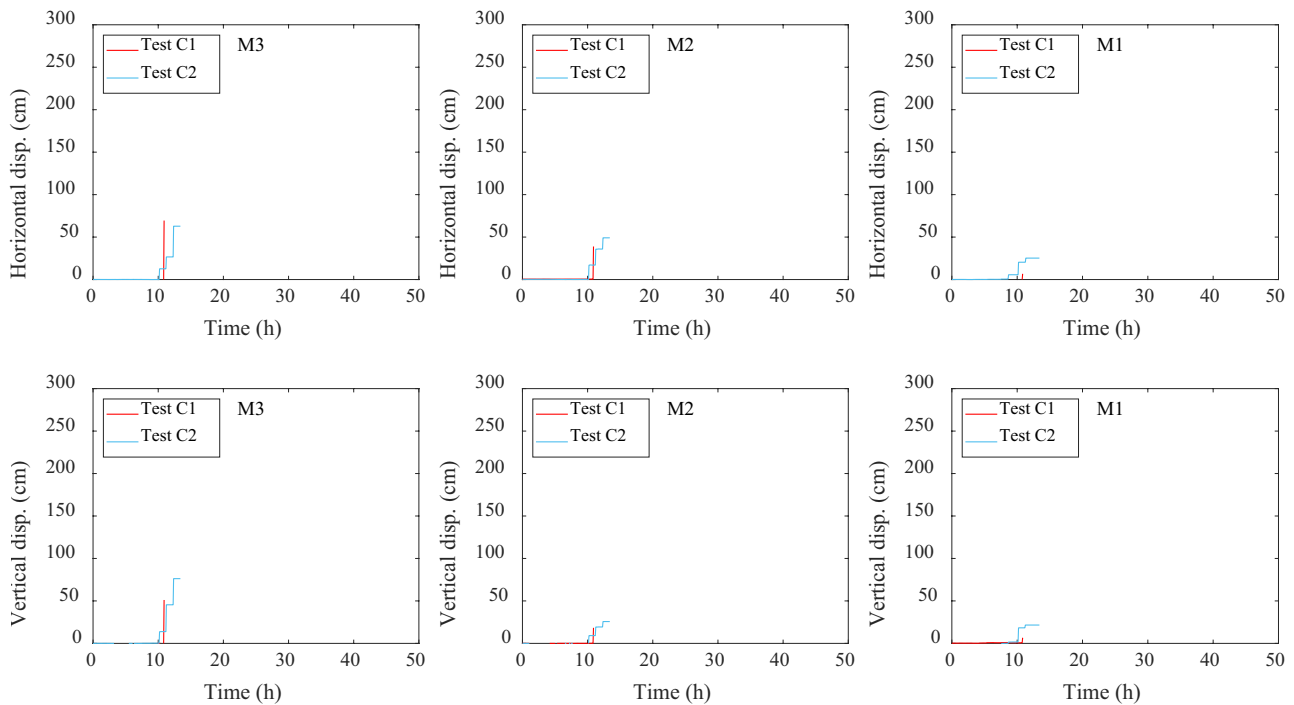

(a) Incremental equivalent strain after shaking in test C1

(c) Incremental equivalent strain at the onset of rainfall-induced landslide in test C1

(b) Incremental equivalent strain after shaking in test C2

(d) Incremental equivalent strain at the onset of rainfall-induced landslide in test C2

Fig. 17 Soil displacement during post-shaking rainfall in tests C1 and C2

In tests C1 and C2, the slopes had the same initial density and water content as those in tests series A and B and once the centrifugal acceleration reached 50 g, rainfall with an intensity of 9 mm/h was released above the centrifuge models for a short period of time, i.e., about 12 s, so the initial degree of saturation of the slopes was increased but no deformation in slopes was found. Then, shaking was excited, after which the same rainfall was restarted and continued until slopes failed. Shaking intensities in two tests were different, as large shaking (4.6 m/s² in the prototype scale) was given to test C1 while small shaking (3.0 m/s² in the prototype scale) was given to test C2.

Slope deformation

Figure 16 illustrates slopes' incremental equivalent strains caused by shaking and its following rainfall in two cases. Shaking with a higher intensity resulted in larger slope deformation, as reflected in the higher strain level and the clear location of crest cracks, according to Fig. 16a, b. The intensified slope deformation then enhanced slope deformation caused by the following rainfall, as demonstrated in Fig. 16c, d. Thus, even under the same rainfall, the slope could have different deformations, which were determined by the shaking prior to rainfall. It could be concluded that slope deformation during post-shaking rainfall also depended on the intensity of pre-rainfall shaking.

During rainfall, the slopes slid along the shaking-caused slip surface and this phenomenon was more significant when the shaking intensity was higher. Comparison between Fig. 16c, d demonstrated that the zone where concentrated strains developed was the same in both cases, regardless of the prior shaking. Also, the intense shaking made the slip surface within the slope much more pronounced, as indicated by the concentration of large strains in Fig. 16a, so that

the following rainfall could further promote deformation within the same zone. Thus, the shaking-induced slope deformation controlled the slip surface location of the slope during the subsequent rainfall.

Landslide kinematics

Figure 17 presents soil displacement during the post-shaking rainfall in two cases. The kinematics of landslide caused by rainfall could be examined through the time history of soil displacement. In spite of the previous shaking with two different intensities, the soil displacement in two cases was comparable, suggesting the total landslide displacement was similar regardless of shaking.

However, the slope in test C1 that experienced larger shaking showed sudden and fast soil movement during rainfall. The soil displacement indicated by the red lines in Fig. 17 suddenly increased to a high level and the failure was instant in test C1, characterizing a landslide with a velocity between "very rapid (50 mm/s)" and "extremely rapid (5 m/s)" (Cruden and Varnes 1996). For the slope in test C2, however, its velocity was much smaller than the velocity of the landslide in test C1. Thus, the shaking intensity directly affected the velocity of the subsequent rainfall-induced landslide and a larger shaking intensity could lead to a faster landslide that was caused by the post-shaking rainfall.

Conclusions

Three series of centrifuge tests on 1:50 scale model slopes have been carried out to examine the response of slopes subject to rainfall with different intensities when they were exposed to antecedent shaking and evaluate the corresponding landslide-triggering mechanisms. Primary conclusions were summarized here.

1. Shaking-induced crest cracks on the slope were near its shoulder, and the existence of cracks greatly affected the slope behavior during the following rainfall.

2. The failure pattern of the slope with cracks during rainfall was significantly different from that displayed by the slope without cracks. When shaking struck the slope and produced cracks on its shoulder and rupture line below, the mobilized soil slid along the slip surface that extended to the rupture line, and once the slope was subjected to a subsequent rainfall event, the main crack became the initial crown of the main scarp, and the progression of the landslide was related to the rainfall intensity.

3. The effect of preferential flow due to the presence of cracks was more evident during rainfall with a greater intensity.

4. Heavy rainfall greatly accelerated the failure of the slope with shaking-induced cracks, resulting in a rapid and massive landslide.

5. Under heavy rainfall, the volume of the displaced material and the area of the main scarp on the upper edge as well as the zone of accumulation were larger in the landslide of the slope with shaking-induced cracks, in comparison with those in the crack-free slope.

6. Under light rainfall, the landslide took place in front of the main crack in the crack-containing slope and developed downslope, making the main scarp on the upper edge expose itself in the vertically downward direction, whereas the ground behind the main crack remained undisturbed throughout the whole process.

7. Once shaking caused tensile cracks on the slope crest, the slope deformation pattern during the following rainfall was closely controlled by the rainfall intensity.

8. The evolution of the factor of safety during rainfall revealed the decreasing stability of slope in each test and the approximated factor of safety could be used for a preliminary estimation of slope stability during rainfall, but a more detailed model was needed for the more accurate assessment of slope stability.

9. For the slopes containing shaking-induced cracks, even though being subjected to the same rainfall, they showed different deformation magnitudes. The slope that experienced larger antecedent shaking had more deformation during rainfall, and the previous shaking-induced slope deformation controlled the slip surface location.

10. The velocity of rainfall-caused landslide could be greatly influenced only because of the prior shaking event. Despite a low intensity, the rainfall could still lead to an instant landslide once the slope has encountered intense antecedent shaking.

One direct implication from the experimental results is that remedies, such as covering the cracks or grouting to prevent preferential flow along the cracks and placing drains at the slope toe area, are required once an earthquake strikes a slope or embankment and gives rise to tensile cracks or fissures. Furthermore, the countermeasure of surface drainage to divert excess water away is also essential to maintain slope stability. Consequently, it will be effective to prohibit or restrain the occurrence of abrupt landslide and obtain sufficient time for the evacuation of people living near the bottom of the slope.

In future studies, the effect of shaking intensity on the generation of cracks on the slope crest needs to be further considered, and more candidate rainfall intensities should be examined in the model tests so that the effect of shaking-induced cracks on water infiltration into slopes can be investigated thoroughly.

References

Atkinson JH, Bransby PL (1978) The mechanics of soils: an introduction to critical state soil mechanics. McGraw-Hill Book Company (UK) Limited, London

Barry DA, Lisle IG, Li L, Prommer L, Parlange JY, Sander GC, Griffioen JW (2001) Similitude applied to centrifugal scaling of unsaturated flow. Water Resour Res 37(10):2471–2479. https://doi.org/10.1029/2000WR000049

Bear J (1972) Dynamics of fluids in porous media. Dover, Mineola, New York

Bhattacherjee D, Viswanadham BVS (2018) Design and performance of an in-flight rainfall simulator in a geotechnical centrifuge. Geotech Test J 41(1):72–91. https://doi.org/10.1520/GTJ20160254

Bishop AW, Morgenstern N (1960) Stability coefficients for earth slopes. Geotechnique 10(4):129–150. https://doi.org/10.1680/geot.1960.10.4.129

Bryant SK, Take WA, Bowman ET, Millen MD (2015) Physical and numerical modelling of dry granular flows under Coriolis conditions. Geotechnique 65(3):188–200. https://doi.org/10.1680/geot.13.P.208

Cai F, Ugai K (2004) Numerical analysis of rainfall effects on slope stability. Int J Geomech 4(2):69–78. https://doi.org/10.1061/(ASCE)1532-3641(2004)4:2(69)

Cargill KW, Ko H (1983) Centrifugal model of transient water flow. J Geotech Eng 109(4):536–555

Chen G, Meng X, Qiao L, Zhang Y, Wang S (2018) Response of a loess landslide to rainfall: observations from a field artificial rainfall experiment in Bailong River Basin. China Landslides 15(5):895–911. https://doi.org/10.1007/s10346-017-0924-6

Chigira (2012) Catastrophic landslides of pyroclastics induced by the 2011 off the Pacific Coast of Tohoku Earthquake. Proceedings of the International Symposium on Earthquake-Induced Landslides, 7–9 November 2012. Kiryu, Japan, pp 139–147. https://doi.org/10.1007/978-3-642-32238-9_15

Chigira M, Yagi H (2006) Geological and geomorphological characteristics of landslides triggered by the 2004 Mid Niigta prefecture earthquake in Japan. Eng Geol 82(4):202–221. https://doi.org/10.1016/j.enggeo.2005.10.006

Cho SE, Lee SR (2001) Instability of unsaturated soil slopes due to infiltration. Comput Geotech 28(3):185–208. https://doi.org/10.1016/S0266-352X(00)00027-6

Conte E, Troncone A (2012) A method for the analysis of soil slips triggered by rainfall. Geotechnique 62(3):187–192. https://doi.org/10.1680/geot.8.P.075

Cornforth (2005) Landslides in practice: investigation, analysis, and remedial/preventative options in soils. John Wiley & Sons Inc., Hoboken, New Jersey

Crosta GB (2004) Introduction to the special issue on rainfall-triggered landslides and debris flows. Eng Geol 73(3–4):191–192. https://doi.org/10.1016/j.enggeo.2004.01.004

Cruden DM, Varnes DJ (1996) Landslide types and processes. In: Turner AK, Schuster RL (eds) Landslides: Investigation and Mitigation. National Academy Press, Washington, DC, pp 36–75

Dell'Avanzi E, Zornberg JZ, Cabral AR (2004) Suction profiles and scale factors for unsaturated flow under increased gravitational field. Soils Found 44(3):79–89. https://doi.org/10.3208/sandf.44.3_79

Duncan JM, Wright SG, Brandon TL (2014) Soil strength and slope stability. John Wiley & Sons Inc, Hoboken

Egawa T, Yamanashi T, Tomisawa K (2018) Study on liquefaction characteristics of volcanic ash soil-report on field investigation in Hokkaido. JAEE J 18(3):104–118. https://doi.org/10.5610/jaee.18.3_104

Fredlund DG, Rahardjo H (1993) Soil mechanics for unsaturated soils. Wiley, New York

Hotta N, Kan YH, Wei TH et al (2005) Relationship between slope failures and precipitation before and after the Chi-chi Earthquake investigated using long-term repair records of forestry roads in the National Taiwan University Forest. J Japan Soc of Eros Control Eng 58(1):3–13

Huang YH (2014) Slope stability analysis by the limit equilibrium method: fundamentals and methods. American Society of Civil Engineers, Reston

Iverson RM (2000) Landslide triggering by rain infiltration. Water Resour Res 36(7):1897–1910. https://doi.org/10.1029/2000WR900090

Geospatial Information Authority of Japan (2016) Kumamoto Earthquake. http://www.gsi.go.jp/BOUSAI/H27-kumamoto-earthquake-index.html

Jackson RD (1972) On the calculation of hydraulic conductivity. Soil Sci Soc Am Proc 36:380–383. https://doi.org/10.2136/sssaj1972.03615995003600020047x

Kameda J, Kamiya H, Masumoto H, Morisaki T, Hiratsuka T, Inaoi C (2019) Fluidized landslides triggered by the liquefaction of subsurface volcanic deposits. Sci Rep 9:13119. https://doi.org/10.1038/s41598-019-48820-y

Keefer DK (1984) Landslides caused by earthquakes. Geol Soc Am Bull 95:406–421

Khattak GA, Owen LA, Kamp U, Harp EL (2010) Evolution of earthquake-triggered landslides in the Kashmir Himalaya, northern Pakistan. Geomorphology 115(1–2):102–108. https://doi.org/10.1016/j.geomorph.2009.09.035

Koga Y, Matsuo O (1990) Shaking table tests of embankments resting on liquefiable sandy ground. Soils Found 30(4):162–174. https://doi.org/10.3208/sandf1972.30.4_162

Liang L, Knappett JA (2017) Centrifuge modelling of the influence of slope height on the seismic performance of rooted slopes. Geotechnique 67(10):855–869. https://doi.org/10.1680/jgeot.16.P.072

Lin C, Shieh C, Yuan B, Shieh Y, Liu S, Lee S (2004) Impact of Chi-Chi earthquake on the occurrence of landslides and debris flows: example from the Chenyulan River watershed, Nantou. Taiwan Eng Geol 71(1–2):49–61. https://doi.org/10.1016/S0013-7952(03)00125-X

Lin C, Liu S, Lee S, Liu C (2006) Impacts of the Chi-Chi earthquake on subsequent rainfall-induced landslides in central Taiwan. Eng Geol 86(2–3):87–101. https://doi.org/10.1016/S0013-7952(03)00125-X

Ling S, Chigira M (2020) Characteristics and triggers of earthquake-induced landslides of pyroclastic fall deposits: an example from Hachinohe during the 1968 M7.9 Tokachi-Oki earthquake. Japan Eng Geol 264:1–11. https://doi.org/10.1016/j.enggeo.2019.105301

Matsumaru T, Suga M, Uzuoka R (2012) Shaking table test of embankment on inclined ground affected by rainfall. Proceedings of International Symposium on Earthquake-Induced Landslides, 7–9 November 2012. Kiryu, Japan, pp 437–444. https://doi.org/10.1007/978-3-642-32238-9_46

Matsuo O, Saito Y, Sasaki T, Kondoh K, Sato T (2002) Earthquake-induced flow slides of fills and infinite slopes. Soils Found 42(1):89–104. https://doi.org/10.3208/sandf.42.89

Mhaske SN, Pathak K, Basak A (2019) A comprehensive design of rainfall simulator for the assessment of soil erosion in the laboratory. CATENA 172:408–420. https://doi.org/10.1016/j.catena.2018.08.039

Montrasio L, Valentino R (2004) Experimental analysis and modelling of shallow landslides. Landslides 4(3):291–296. https://doi.org/10.1007/s10346-007-0082-3

Ng CWW, Zhan LT, Bao CG, Fredlund DG, Gong BW (2003) Performance of an unsaturated expansive soil slope subjected to artificial rainfall infiltration. Geotechnique 53(2):143–157. https://doi.org/10.1680/geot.2003.53.2.143

Ng CWW, Kamchoom V, Leung AK (2016) Centrifuge modelling of the effects of root geometry on transpiration-induced suction and stability of vegetated slopes. Landslides 13(5):925–1938. https://doi.org/10.1007/s10346-015-0645-7

Okada Y, Sassa K, Fukuoka H (2000) Liquefaction and the steady state of weathered granitic sands obtained by undrained ring shear tests: a fundamental study of the mechanism of liquidized landslides. J Nat Dis Sci 22:75–85. https://doi.org/10.2328/jnds.22.75

Owen L, Kamp U, Khattak GA, Harp E, Keefer D, Bauer MA (2008) Landslides triggered by the 8 October 2005 Kashmir earthquake. Geomorphology 94(1–2):1–9. https://doi.org/10.1016/j.geomorph.2007.04.007

Qi S, Vanapalli SK (2015) Hydro-mechanical coupling effect on surficial layer stability of unsaturated expansive soil slopes. Comput Geotech 70:68–82. https://doi.org/10.1016/j.compgeo.2015.07.006

Rahardjo H, Lee TT, Leong EC, Rezaur RB (2005) Response of a residual soil slope to rainfall. Can Geotech J 42(2):340–351. https://doi.org/10.1139/t04-101

Rezzoug A, Konig D, Triantafyllidis T (2004) Scaling laws for centrifuge modeling of capillary rise in sandy soils. J Geotech Geoenviron Eng 130(6):615–620. https://doi.org/10.1061/(asce)1090-0241(2004)130:6(615)

Richards LA (1931) Capillary Conduction of liquids through porous mediums. Physics 1:318–333. https://doi.org/10.1063/1.1745010

Sassa K, Fukuoka H, Scarascia-Mugnozza G, Evans S (1996) Earthquake-induced-landslides: distribution, motion and mechanisms. Soils Found 36:53–64. https://doi.org/10.3208/sandf.36.Special_53

Sassa K, Tsuchiya S, Fukuoka H, Mikos M, Doan L (2015) Landslides: review of achievements in the second 5-year period (2009–2013). Landslides 12(2):213–223. https://doi.org/10.1007/s10346-015-0567-4

Sato HP, Hasegawa H, Fujiwara S, Tobita M, Koarai M, Une H, Iwahashi J (2007) Interpretation of landslide distribution triggered by the 2005 Northern Pakistan earthquake using SPOT 5 imagery. Landslides 4(2):113–122. https://doi.org/10.1007/s10346-006-0069-5

Schuster RL, Nieto AS, O'Rourke TD, Crespo E, Plaza-Nieto G (1996) Mass wasting triggered by the 5 March 1987 Ecuador earthquakes. Eng Geol 42(1):1–23. https://doi.org/10.1016/0013-7952(95)00024-0

Seed HB (1966) Slope stability during earthquakes. J Soil Mech Found Div 93(4):299–323

Seed HB, Goodman RE (1964) Earthquake stability of slopes of cohesionless soils. J Soil Mech Found Div 90(6):43–73

Sharma RH, Nakagawa H (2010) Numerical model and flume experiments of single- and two-layered hillslope flow related to slope failure. Landslides 7(4):425–432. https://doi.org/10.1007/s10346-010-0205-0

Springman SM, Thielen A, Kienzler P, Friedel S (2013) A long-term field study for the investigation of rainfall-induced landslides. Geotechnique 63(14):1177–1193. https://doi.org/10.1680/geot.11.P.142

Take WA, Beddoe RA, Davoodi-Bilesavar R, Phillips R (2015) Effect of antecedent groundwater conditions on the triggering of static liquefaction landslides. Landslides 12(3):469–479. https://doi.org/10.1007/s10346-014-0496-7

Take WA, Bolton MD, Wong PC, Yeung FJ (2004) Evaluation of landslide triggering mechanism in model fill slopes. Landslides 1(3):173–184. https://doi.org/10.1007/s10346-004-0025-1

Tamate S, Suemasa N, Katada T (2012) Simulation of precipitation on centrifuge models of slopes. Int J Phys Model Geotech 12(3):89–101. https://doi.org/10.1680/ijpmg.11.00009

Tang C, Zhu J, Qi X, Ding J (2011) Landslides induced by the Wenchuan earthquake and the subsequent strong rainfall event: a case study in the Beichuan area of China. Eng Geol 122(1–2):22–33. https://doi.org/10.1016/j.enggeo.2011.03.013

Taylor RN (1995) Geotechnical centrifuge technology. Blackie Academic and Professional, Glasgow

Tomita Y, Sukurai W, Naka N (1996) Study on the extension of collapse caused by rainfall after the earthquake in Rokko Mountain Range. J Japan Soc Eros Control Eng 48(6):15–21. https://doi.org/10.11475/sabo1973.48.6_15

Tian D, Zhen H, Liu D (2017) A 2D integrated FEM model for surface water–groundwater flow of slopes under rainfall condition. Landslides 14(2):577–593. https://doi.org/10.1007/s10346-016-0716-4

Tristancho J, Caicedo B, Thorel L, Obregon N (2012) Climatic chamber with centrifuge to simulate different weather conditions. Geotech Test J 35(1):159–171. https://doi.org/10.1520/GTJ103620

Usui Y, Shimada H, Innami H, Amao H, Higashi K, Kawabata H (2013) Case study on heavy rainfall-induced reactivation of seismically disturbed slope caused by the 2011 off the Pacific Coast of Tohoku Earthquake. In: Ugai K, Yagi H, Wakai A (eds) Earthquake-Induced Landslides. Springer, Berlin, Heidelberg, pp 323–329. https://doi.org/10.1007/978-3-642-32238-9_33

Uzuoka R, Sento N, Kazama M, Unno T (2005) Landslides during the earthquakes on May 26 and July 26, 2003 in Miyagi. Japan Soils Found 45(4):149–163. https://doi.org/10.3208/sandf.45.4_149

Uzuoka R, Borja RI (2012) Dynamics of unsaturated poroelastic solids at finite strain. Int J Numer Anal Meth Geomech 36:1535–1573. https://doi.org/10.1002/nag.1061

van Genuchten MT (1980) A closed-form equation for predicting the hydraulic conductivity of unsaturated soils. Soil Sci Soc Am J 44:892–898. https://doi.org/10.2136/sssaj1980.03615995004400050002x

Wang G, Suemine A, Zhang F, Hata Y, Fukuoka H, Kamai Y (2014) Some fluidized landslides triggered by the 2011 Tohoku Earthquake (Mw 9.0). Japan Geomorphology 208:11–21. https://doi.org/10.1016/j.geomorph.2013.11.009

Wang F, Fan X, Yunus AP, Subramanian S, Alonso-Rodriguez A, Dai L, Xu Q, Huang R (2019) Coseismic landslides triggered by the 2018 Hokkaido, Japan (Mw 6.6), earthquake: spatial distribution, controlling factors, and possible failure mechanism. Landslides 16(8):1551–1566. https://doi.org/10.1007/s10346-019-01187-7

Wang G, Sassa K (2001) Factors affecting rainfall-induced fowslides in laboratory flume tests. Geotechnique 51(7):587–599. https://doi.org/10.1680/geot.2001.51.7.587

Wu LZ, Zhang LM (2009) Analytical solution to 1D coupled water infiltration and deformation in unsaturated soils. Int J Numer Anal Meth in Geomech 33(6):773–790. https://doi.org/10.1002/nag.742

Xiong Y, Bao X, Ye B, Zhang F (2014) Soil-water-air fully coupling finite element analysis of slope failure in unsaturated ground. Soils Found 54(3):377–395. https://doi.org/10.1016/j.sandf.2014.04.007

Zhang W, Askarinejad A (2019) Centrifuge modelling of submarine landslides due to static liquefaction. Landslides 16(10):1921–1938. https://doi.org/10.1007/s10346-019-01200-z

Zhang G, Qian J, Wang R, Zhang JM (2011) Centrifuge model test study of rainfall-induced deformation of cohesive soil slopes. Soils Found 51(2):297–305. https://doi.org/10.3208/sandf.51.297

Zhang LL, Fredlund DG, Fredlund MD, Wilson GW (2014) Modeling the unsaturated soil zone in slope stability analysis. Can Geotech J 51:1384–1398. https://doi.org/10.1139/cgj-2013-0394

Jiawei Xu (✉)
Department of Civil and Earth Resources Engineering, Kyoto University, Gokasho, Uji, Kyoto 611–0011, Japan
Email: xu.jiawei.38z@st.kyoto-u.ac.jp

Kyohei Ueda · Ryosuke Uzuoka
Disaster Prevention Research Institute, Kyoto University, Kyoto 611–0011, Japan

Kyohei Ueda
Email: ueda.kyohei.2v@kyoto-u.ac.jp

Ryosuke Uzuoka
Email: uzuoka.ryosuke.6z@kyoto-u.ac.jp